Type- and Species-Selective Air Etching of Single-Walled Carbon Nanotubes Tracked with *in Situ* Raman Spectroscopy

Andrew Li-Pook-Than,[†,‡] Jacques Lefebvre,[†] and Paul Finnie[†,‡,*]

[†]National Research Council Canada, Building M-50, 1200 Montreal Road, Ottawa, ON, K1A 0R6, Canada and [‡]Department of Physics, University of Ottawa, 150 Louis Pasteur, Ottawa, ON, K1N 6N5, Canada. The manuscript was written through contributions of all authors. All authors have given approval to the final version of the manuscript. A.L. performed the experiments, P.F. and A.L. planned the experiments, and all authors contributed to the analysis of the data and the writing of the manuscript.

ABSTRACT The thermal oxidation of carbon nanotubes in air is investigated by *in situ* Raman spectroscopy. Etching rates are directly seen to be diameter, chirality, and type dependent. We directly track the evolution of bundled nanotube networks that undergo air etching from 300 to 600 °C. Some species are more robust than others. Changes to radial breathing mode (RBM) and G− peak structures suggest that metallic species etch away more rapidly, with smaller diameter semiconducting species etching more slowly and large diameter nanotubes, including semiconductors, etching last. The decay in integrated G and D band intensities is tracked and fit reasonably well with biexponential decay. The RBM evolution is better represented by a single exponential. All bands are fit to activation plots with RBMs showing significantly different rates.

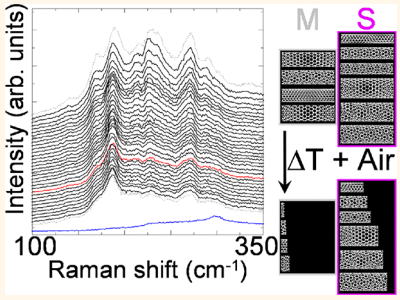

KEYWORDS: carbon nanotube combustion · air etching · *in situ* Raman spectroscopy · purification · chirality

Depending on the situation, the combustion of carbon nanotubes (CNTs) in air can be either detrimental or useful. In synthesis, it can inhibit or counteract growth, and in devices it can limit operating currents and temperatures. Controlled, it is a powerful chemical tool that plays a role in CNT characterization, structure modification, and purification.[1−7] There has recently been a resurgence of interest in the manipulation of nanotube populations *via* oxidation. In this work we will show evidence obtained by *in situ* Raman tracking that combustion is type selective, with potential applications for preparing semiconductor-rich nanotube ensembles. *In situ* Raman provides a unique window on the dynamics of the process, allowing one to track the evolution as it happens and observe trends that might be difficult to detect in static *ex situ* measurements.

Before discussing our experiments, we briefly review aspects of nanotube oxidation and purification. Oxidation is routinely used to characterize CNT purity. The mass and chemical characterization of CNTs and composite materials are commonly studied by techniques such as thermogravimetric analysis and differential thermal analysis, which can involve thermally oxidizing these samples in air.[4,8−12] It is also common to thermally oxidize CNT material in air or oxygen in order to remove defective carbon coatings, expose and/or remove catalyst particles following CNT synthesis, or otherwise modify non-CNT structures in the sample.[7,10,13−16] More generally, gas-phase oxides are frequently used to chemically alter the outcome of a number of CNT growth and separation practices.[13,14,17−23]

Perfect chirality control in nanotube synthesis has not been achieved. However, postprocessing separation and purification processes have been remarkably successful, encompassing an enormous variety of techniques of different yield and complexity.[24] Solution-based sorting is extensively studied, being potentially very high fidelity, relatively scalable, and inexpensive. However, such methods are not without weaknesses: they can be complicated and may be difficult to scale, and preparation of solutions typically damages nanotubes and coats them with difficult-to-remove adsorbates. Gas-phase selectivity would have some compelling advantages. It potentially would not leave residues and could potentially leave

* Address correspondence to paul.finnie@nrc-cnrc.gc.ca.

Received for review October 10, 2012 and accepted July 3, 2013.

Published online July 09, 2013
10.1021/nn402412t

nanotubes in a pristine state.[2,6] Recently there has been a resurgence of interest in oxidative etching and its selectivity, especially with respect to semiconducting or metal type.[25,26] Furthermore, there is an emerging consensus that etching plays a significant role in selectivity in synthesis, and efforts are being made to harness this.[22,27] So one motivation to explore gas-phase etching is that it can be naturally combined with chemical vapor deposition synthesis.

Air etching is very simple and scalable. However, as we will show, one drawback of air etching is that the selectivity that is presently achievable is relative and all CNTs are destroyed to some extent, such that a large initial mass is required. This is less of a problem now that high-yield synthesis is achievable. This method might one day allow sufficient nanotube separation for some applications. Furthermore, this drawback may not be important if etching is integrated with CVD synthesis.

Oxidation is well known to be effective at selectively burning off nongraphene nanocarbons and removing impurities while leaving behind sp^2 carbon. Reactivity reportedly increases going from graphite to well-graphitized amorphous carbon, to multiwalled CNTs, and then to single-walled CNTs (SWNTs).[8] Fullerenes are even more reactive than CNTs, which is attributed to higher surface curvature.[28] Defective sp^3-hybridized carbon is expected to etch faster than nondefective carbon.[8,29] Furthermore, compared to graphite, oxygen adsorbs onto and dopes carbon nanotubes more easily.[30−32] Osswald *et al.* found that disordered carbon removal by air oxidation was more complete in double-walled CNTs, compared to SWNTs.[33] The controlled oxidation of defective CNT walls has also been used to selectively remove layers from multiwalled CNTs and modify conductivity.[34]

There is already evidence that separation can be achieved by selective CNT destruction using various gas-phase oxidants, including air,[1,6] O_2 gas,[3−5,22,23] SO_3,[35] hydrogen plasma,[36] methane plasma,[37] water vapor,[27] and fluorine gas.[38] In all these studies, etching rates were found to increase with smaller CNT diameter (d_t), although these rates were also often found to be sensitive to CNT chirality. This diameter dependency, also observed in solution-phase oxidation studies,[39,40] is typically explained in terms of higher C−C bond strain, resulting in higher chemical reactivity with adsorbates.[1−6,35,37,38,41−43]

While bond strain does scale with diameter to a first approximation, it is the local curvature radius (LCR) that determines the weakest carbon−carbon bond and consequently is thought to be a limiting factor in oxidative etching.[1,44] LCR is chiral angle dependent and smallest for armchair tubes and largest for zigzags, with the result that armchairs should be least robust. This is despite an earlier study having ascribed faster etching to zigzag CNTs.[40] So, in terms of chirality, when etching with air, studies have found that etching rate scaled directly with higher chiral angle (θ) values and explained this in terms of LCR differences.[1,43−45] Miyata *et al.* have explicitly modeled this rate-determining process for chiral angle. These purely geometric arguments predict faster etch rates for small-diameter nanotubes and do not in themselves explain differences in electronic type, *e.g.*, differing etch rates for metallic CNTs (m-CNTs) and semiconducting CNTs (s-CNTs). Doping, however, is expected to be as significant a factor as chiral angle.[1,46] More generally, other studies have shown that chirality is expected to have a direct effect on oxygen sidewall chemisorption and can affect chemical reactivity in general.[47,48]

Depending on the etching gas and the particular treatment, there are already some reports indicating that m-CNTs may etch more rapidly with gas-phase oxidants than s-CNTs.[2,36−38,40,49] Using laser irradiation in air, Huang *et al.* observed both the preferential destruction of m-CNTs and high chiral angle s-CNTs.[50] Similar studies involving the light-induced selective attack of m-CNTs have also been reported.[51,52]

Very recently Lukaszczuk *et al.* claimed on the basis of absorption experiments and Raman data that metallic SWNTs can be selectively etched in open air, such that 95% semiconducting purity can be obtained.[25] Also very recently, Li *et al.* have reported that carbothermic oxidation of nanotubes, obtained by oxidizing nanotubes in air under a NiO layer, results in selective etching of metallic nanotubes.[26] These exciting new results with respect to type-selective oxidation reinforce the promise of such approaches and the value of *in situ* data.

Preferential m-CNT etching has been attributed to different mechanisms in various situations. One factor is the lower enthalpy of formation of semiconductors,[37,53] while another factor may be the presence of delocalized electronic states and separately the smaller ionization potential.[22,26,37,38] The presence of electronic states near the Fermi level for metals and the differences in work function[54,55] between semiconductors and metals are very important for the selectivity of chemical reactions.[26,55−57]

In other studies the opposite trend, with semiconductors being preferentially etched, has been observed, including those involving H_2O_2 as an oxidant.[2,35,40] Kawai *et al.* suggests that this might be due to the C−C bond weakening caused by hole doping.[44] Theoretically, density functional calculations have also suggested that CO_2 gas will preferentially etch non-armchair CNTs.[58]

In situ approaches are especially well suited to investigating such problems, as one can actually track the selectivity of the etching as it happens. Raman spectroscopy is solidly established as a tool that provides detailed information about all aspects of nanotubes and nanocarbon ensembles. In this work, as-grown CNT films on silicon are etched in air and dynamically

characterized using *in situ* Raman spectroscopy, a technique that has been used to monitor CNT growth at high temperature.[59−65] Here, samples are etched at temperatures between 300 and 600 °C, and dynamic changes to ~10 radial breathing mode (RBM) peaks, each corresponding to specific CNT diameter and chiralities, are tracked at all temperatures. The corresponding spectral evolution of the G and D bands is also tracked. At low temperatures, we validate the finding that metallic nanotubes etch faster, producing a semiconductor-enriched sample, and analyze the activation profiles of the G band, D band, and different semiconducting and metallic RBMs. A chirality/diameter (*n*,*m*) dependence also appears to be present, but we were unable to match the data to a single, simple relation with chiral angle. The etching dynamics and the Arrhenius plots of the various modes provide insight into the possible mechanisms of selectivity.

RESULTS AND DISCUSSION

Scanning electron microscope (SEM) images provide a general overview of the sample and the progress of etching. The same sample was imaged and etched in steps to evaluate the progress of etching (Figure 1). The technical details of the etching procedure are listed in the Methods section. Figure 1(a) shows an SEM image prior to etching. The CNTs form a tangled network of thick bundles, with most bundles less than 25 nm wide and occasional individual tubes or small bundles less than 5 nm wide. Essentially no individual SWNTs can be seen: all are bundled. Figure 1(b) shows an image after 30 min of etching at 425 °C. There are fewer stacks of bundles, and the network appears less dense. Individual bundle lengths appear similar, but the bundle thickness may be less uniform. Some bundles appear to be peeling off and forking into thinner bundles. Candidates for individualized SWNTs are visible (diameters <5 nm).

Figure 1(c) shows the corresponding image after a total of 90 min of etching at 425 °C. The surface density of nanotubes has decreased even more, and the bundles are thinner, though they remain present. The sidewalls of the forking bundles appear to be "frayed" and more uneven, while some bundles have been completely severed, although most bundle lengths remain the same. The silicon substrate surface, including the catalyst nanoparticles on the surface, is more exposed in Figure 1(b) than at earlier etching times such as Figure 1(a), where the mat of nanotubes obscures the catalyst nanoparticles. Higher accelerating voltage SEM images also show the presence of surface nanoparticles for all etching times, which would correspond to catalyst particles.

Thus, the overall effect of the air etch is to decrease the CNT film density and to attack along the entire length of the bundles, not only at the end of the bundles. A similar form of sidewall attack is described

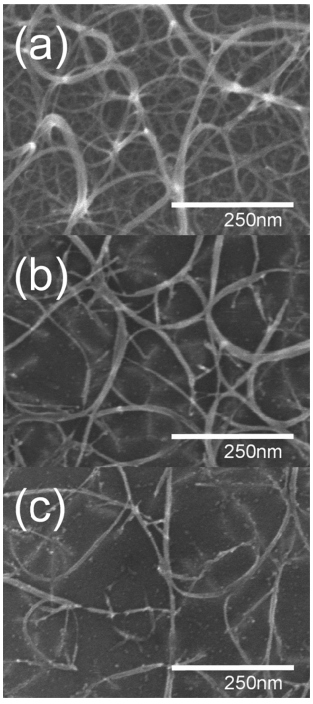

Figure 1. Scanning electron microscope micrographs of sample etched in air: (a) before etching, (b) after 30 min of etching, and (c) after 1 h 30 min of etching. The sample was etched at 425 °C.

by Miyata *et al.*, in which different barrier heights for C−C bond breaking during air combustion are found to be dependent on sidewall curvature.[1] Sidewall attack due to oxidation has also been described in a very recent transmission electron microscope (TEM) study.[66]

Transmission electron microscope images, including high-resolution TEM (HRTEM), of a typical pre-etch sample are included and discussed in the Supporting Information (SI), showing a similar configuration of primarily bundled nanotubes, with a smaller number of isolated SWNTs. From the TEM and SEM micrographs, we notice that the surface of the nanotube bundles appears to be relatively free of any large deposits of amorphous carbon. The HRTEM images reveal that bundles are very clean, and isolated SWNTs appear uncoated. There are certainly no large deposits of unstructured carbon; however, we cannot rule out the presence of intimately associated graphitic-like coatings, which are likely to be present at least to some extent.

In addition to TEM, X-ray photoelectron spectroscopy (XPS) was also performed to better characterize any non-nanotube carbon on pre-etch samples. A typical XPS spectrum is included in the SI. The asymmetric and narrow 1s C peak is essentially dominated by sp^2 carbon, consistent with the CNTs being relatively pristine and having very limited amounts of amorphous or defective carbon present.

The progress of the etching was tracked by *in situ* Raman spectroscopy. Figure 2 shows the *in situ* Raman

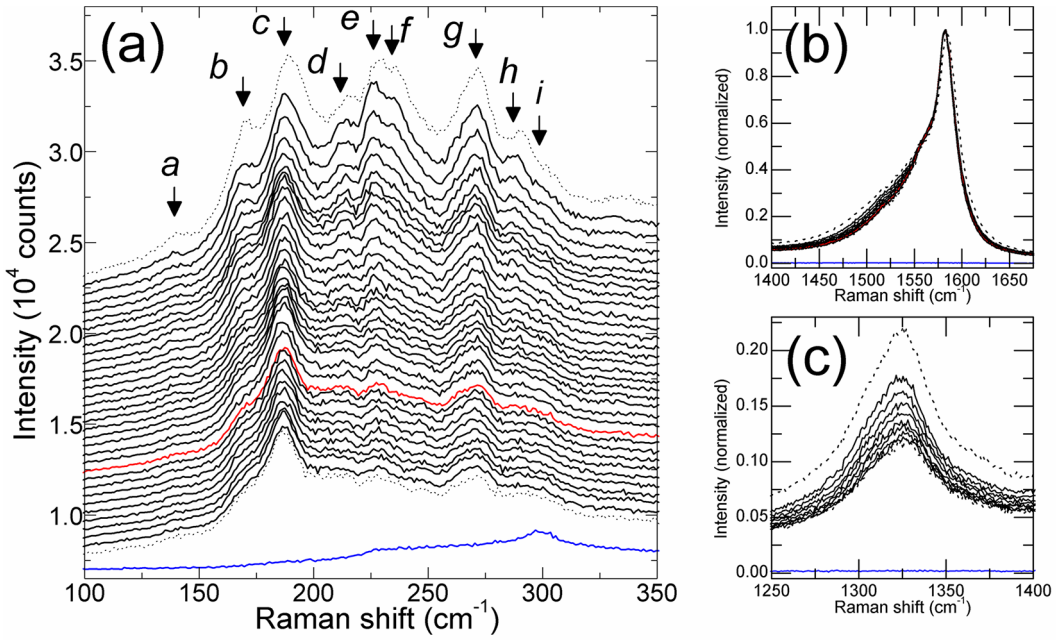

Figure 2. *In situ* **Raman spectra of a sample being etched at 350 °C, displayed chronologically from top to bottom. (a) Spectral changes in the RBM region. Spectra have been offset for clarity. Also shown are corresponding changes to (b) G and (c) D bands. These spectra are not offset. The top and bottom dotted spectra correspond respectively to pre- and post-etch spectra (after t = 132 min) for the sample. The corresponding Si/SiO_2 backgrounds are displayed in blue. In (a) spectra are shown every 4 min, from t = 4 min to t = 128 min, with air input occurring at t = 0 s (the original frames were taken with 5 s exposure every 10 s and then binned over 2 min). In (b) and (c) every spectrum is normalized to their maximum G band intensity. In (b) and (c), spectra are shown every 16 min, from t = 16 min to t = 128 min. The Raman excitation wavelength for all spectra was 532 nm.**

spectra of a typical sample etched at 350 °C. Figure 2(a) shows the spectral region of RBMs and their time evolution in 4 min intervals. The spectra are shown in chronological order, from top to bottom, with the top spectrum corresponding to conditions before air is first flowed into the reactor. In Figure 2(a) the spectra are slightly offset vertically to make tracking the RBMs easier. The most prominent RBMs appear to be visible on all samples both at room temperature and when heated. There are changes in peak intensity with heating, as expected due to the softening of the modes themselves, as well as the gradual shift in the energy of the resonant level that occurs when materials are heated. These RBMs experience an expected[67] frequency downshift of 3 cm^{-1} to 7 cm^{-1} with respect to their room-temperature frequencies when the given sample is heated from room temperature to temperatures between 300 and 600 °C.

We label nine of the most intense peaks in Figure 2(a), namely, the peaks centered at (*a*) 143 cm^{-1}, (*b*) 171 cm^{-1}, (*c*) 189 cm^{-1}, (*d*) 216 cm^{-1}, (*e*) 228 cm^{-1}, (*f*) 236 cm^{-1}, (*g*) 272 cm^{-1}, (*h*) 290 cm^{-1}, and (*i*) 303 cm^{-1}. On the basis of peak width and asymmetry, some of these peaks may represent more than one RBM.[68] For example, peak *c* contains at least RBMs at 187 and 189 cm^{-1}. The intensity of peak *a* is reduced due to a drop in the transmission caused by the optical setup at this and lower wavenumbers. All RBM peaks are superimposed on a distinctive silicon/silicon dioxide background signal (blue spectrum).

As discussed, early work indicates that smaller diameter nanotubes burn first, followed by large-diameter nanotubes.[39,41] Since the RBM frequency is nearly inversely proportional to diameter, RBM peaks at higher Raman shift are expected to burn before those at smaller RBM energies. This general trend does seem to be present in our data, with, for example, peak *i* etching faster than peak *c*. However, that is clearly only a rough approximation, and the true evolution is more subtle than just small diameter burning faster than large diameter.

Most notably, peak *c* remains resistant to etching compared to all other peaks. So, although a large proportion of the nanotubes are burned off (*i.e.*, ~55% of the G band intensity is lost), the residue is relatively "enriched" with the RBM *c* nanotubes after etching (*i.e* the relative intensity of RBM *c* has increased by more than twice when compared to total RBM intensity).

At the outset (t = 0 s) the relative intensities of peak *c* *versus* peaks *e* and *f* are comparable. However, by t = 92 min (red spectrum) peaks *e* and *f* can no longer be clearly distinguished, while peak *c* has undergone relatively less etching. Importantly, the larger diameter peak *b* also etches faster than peak *c*, with the peak *b* shoulder having almost vanished at this time as well, meaning that we have more than just diameter dependence. A more subtle change also occurs within the first 2 min of etching, such that the center of peak *c* moves from 189 cm^{-1} to 187 cm^{-1} and stays there

until etching is stopped, suggesting that two RBM populations with similar diameters can etch at substantially different rates.

Peak *g* similarly appears to resist etching compared to other peaks, albeit not as much as peak *c*. That is, prior to etching peak *g* is comparable in intensity to peak *c*, but after stopping the etching, peak *c* is at least twice the intensity of peak *g*. More generally, peaks *d* to *f* appear to etch faster than the smaller diameter peaks *g* to *i*, while both of these groups etch faster than peak *c*. Again, pure diameter dependence cannot explain this group behavior.

Assignment to chiralities can be performed with reference to a Kataura plot. Most of the pre-etch RBM peaks at room temperature remain clearly visible as the samples are heated to their etching temperatures, so despite changes to peak intensity and frequency, chiral assignments made at room temperature and etching temperatures are essentially the same.[67] For small-diameter nanotubes there are only a few possible chiralities, and above ~250 cm^{-1} a robust assignment is possible. At smaller Raman shifts the assignment can only be tentative. However, the peaks can be naturally grouped into semiconducting and metallic types; see SI for details. Qu *et al*. applied a similar grouping technique when analyzing the selective growth of s-CNTs *vs* plasma CVD.[69] From the SI it is very likely that peaks *g* to *i* correspond to semiconducting (E_{22}^{S} excitonic transition energy) species, with the most likely chiral assignments being *g* 272 cm^{-1} (8,4), *h* 290 cm^{-1} (9,2), and *i* 303 cm^{-1} (6,5). Peaks *d* to *f* correspond to metallic (E_{11}^{M}) species, with some possible chiral assignments being *d* 216 cm^{-1} (8,8), (12,3), or (13,1), *e* 228 cm^{-1} (9,6), and *f* 236 cm^{-1} (10,4). Peaks *b* and *c* correspond either to metallic (E_{11}^{M}) or semiconducting (E_{33}^{S}) species, and chiral assignments are uncertain because of the crowding of different possibilities in the Kataura plot. However, the resistant peak *c* could very well correspond to (16,0), a semiconducting zigzag species. The low-intensity peak *a* corresponds to a semiconducting species: (E_{33}^{S}) or (E_{44}^{S}). In terms of type, it is normal for a fixed wavelength slice of the Kataura plot to break down this way, with metallic peaks in the middle and semiconducting peaks on either side. This assignment suggests that the SWNT populations that etch the fastest correspond to metallic species.

Further information about the evolution of the ensemble comes from the G and D band evolution. Both bands decrease with time as material is etched away. Changes to the G and D bands for the sample etched at 350 °C are shown in Figure 2(b,c). Spectra are shown at 16 min intervals, and all spectra have been normalized to a peak G band intensity of unity.

The G band line shape contains information about diameter and metallicity (*i.e.*, semiconductor/metal ratios). The G band for a single nanotube is made up of a G+ at around 1590 cm^{-1} and the G− at smaller Raman shifts, and ensembles such as these are a superposition of many individual G+ and G− peaks. The G− peak position is diameter dependent and can be used in an analogous way as the RBM to determine diameter.[70,71] The further to the left the G− is, the smaller the CNT diameter. However, unlike the smaller energy RBM modes, the G− to G+ spacing depends on whether the tubes are metallic or not. For a fixed diameter, a metallic G− is approximately twice as far in energy from the G+ for a semiconductor.[71,72] A 1 nm diameter semiconducting nanotube has a G− at about 1550 cm^{-1},[70] whereas a metallic tube of the same diameter is at about 1510 cm^{-1}.[71,72] The resonance window for G bands is broader than for RBMs (about 300 meV compared to about 100 meV),[70] meaning that resonance conditions are not as strict for G bands.

The G+ band is the strongest peak in Figure 2(b), and normalized to its peak intensity, it appears to show essentially no change, apart from its initial 2 cm^{-1} downshift. The G−, on the other hand, changes significantly. In the G−, there is a gradual loss of intensity for small wavenumbers (below ~1555 cm^{-1}), suggesting a decrease in smaller diameter nanotubes. But this loss also indicates a change in metallicity. Importantly, below about 1490 cm^{-1} there is practically no contribution from semiconducting nanotubes, as they would be smaller than 0.5 nm in diameter and so would not be stable.[70,71] Therefore, any G− intensity to the left of this point can be attributed only to metallic nanotubes. There is a substantial loss of spectral intensity in this region. Furthermore, the decrease is relatively uniform from 1425 cm^{-1} to 1525 cm^{-1}. This suggests that the etching throughout this region is primarily metallic etching over a broad range of diameters.

The loss in G− broadness is consistent with the RBM region loss of peaks *e* and *f* if they are metallic peaks, as proposed. The loss in lower frequency G− peaks is also consistent with the initial loss of small-diameter nanotubes present in the RBM. The G− band evolution is an independent line of evidence that supports the contention that the air has preferentially etched metallic nanotubes. This is in contrast to the very recent selective oxidation report of Lukaszczuk *et al*., where there is little obvious change in the G− features.[25] The reason for the apparent lack of G band evolution in their work is not entirely clear; certainly the G band shape should change if the semiconductor to metallic ratios changes, provided both types are resonant. By contrast, studies involving the etching of m-SWNTs using microwave irradiation with mixed-acid-assisted dispersion[73] as well as fluorine gas[38] and oxygen gas[23] did show a significant change in G− structure, as expected. Also, unlike the work of Lukaszczuk *et al*., we never observe the reappearance of new small-diameter, semiconducting RBMs, an intriguing outcome of that work.

The D band gives information about the evolution of crystallinity and the degree of bundling. In Figure 2(c) the D band evolution is shown normalized to the G band peak intensity. Over the entire 132 min etching time, the D/G ratio drops by about a factor of 2, likely indicating that the crystallinity of the remaining nanotubes is higher than the starting material, as expected.[33] The time evolution of the D/G integrated peak intensity ratios for samples etched at different temperatures is given in the SI. Lower, improved D/G ratios can be obtained by etching the samples longer. For example, for the 350 °C sample, the initial D/G is *ca.* 0.12, and this value falls to D/G ≈ 0.08 when 50% of the carbon is etched, as estimated by the reduction in G band intensity.

In Figure 2(c) the D band is composed of at least two peaks centered at around 1324 and 1355 cm^{-1}. These likely correspond to bundled *versus* unbundled nanotube populations, respectively, although for isolated SWNTs the D band has been seen to be somewhat sensitive to CNT diameter.[74] Since the scaled D band line shape changed little over the course of the etching and shows only a gradual shift in spectral weight to small Raman shifts, this implies that the amount of bundling has not changed significantly and has probably not had a significant effect on D/G ratio.

A separate example of etching performed at a higher temperature, in which the sample is more completely etched, is shown in the SI. At late times even the etch-resistant bands are destroyed, which indicates that there is a compromise between selectivity and yield, and the best situation will be obtained at some intermediate amount of etching. However, because a more complete etching is achieved, the defect density is reduced significantly. The D/G ratio continues to drop below even 1% of its initial value, although the G band is still easily detectable. The G band line shape is indicative of large-diameter semiconducting nanotubes remaining at the end. Partial etching in this way is therefore usable to obtain highly defect free large-diameter SWNTs.

More generally, there appears to be little or no change in the amount of type selectivity or species selectivity over the range T = 300 to 400 °C, for a fixed amount of G band etching. Thus a wide temperature range is usable for this type of selectivity, with mainly the rate increasing as the temperature is increased. Above 400 °C, the evolution seems similar; however the changes take place too fast and our data were not good enough to determine convincingly whether or not the degree of selectivity had changed at these high temperatures.

Room-temperature Raman spectra provide another perspective on the changes caused by air etching. Figure 3 shows the room-temperature spectra of a sample that was etched at 550 °C, such that the pre-etch (black) and post-etch (red) spectra are displayed. A scaled-up version of the post-etch spectrum (green)

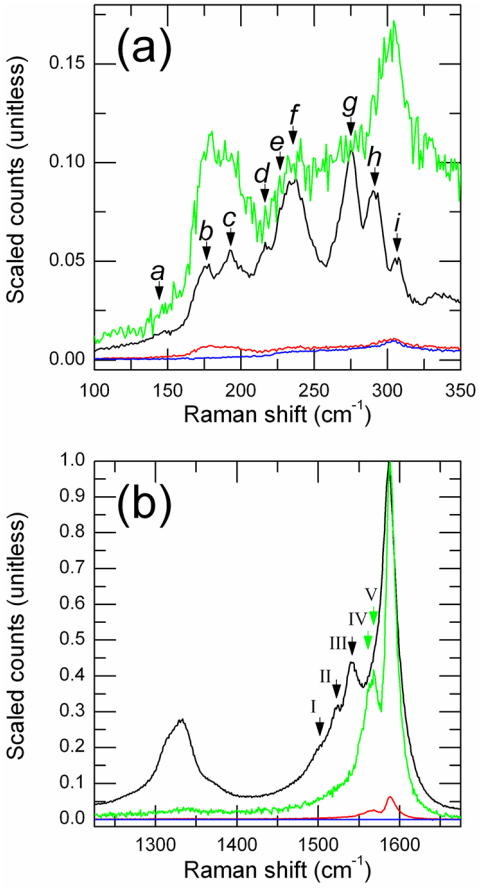

Figure 3. Room-temperature pre-etch Raman spectra (black), with corresponding post-etch (red) spectra and Si/SiO_2 background (blue). The (a) RBMs and (b) G and D bands are shown. The intensity is normalized so that the pre-etched maximum G band peak intensity is unity. The post-etch spectrum is also shown normalized to the post-etch G maximum (green). The peak on the blue, green, and red curves near 300 cm^{-1} is from the substrate. The sample was etched at 550 °C (with 6 × 5 s exposures).

is also shown, such that the G+ matches that of the pre-etch spectrum in order to contrast the change in G band structure. Prior to etching, most of the RBMs visible at high temperature remain visible at room temperature, although they are shifted and at different relative intensities. As indicated in Figure 3(a), we have *a* 145 cm^{-1}, *b* 177 cm^{-1}, *c* 192 cm^{-1}, *d* 217 cm^{-1}, *e* 230 cm^{-1}, *f* 236 cm^{-1} (possibly at 242 cm^{-1}), *g* 273 cm^{-1}, *h* 290 cm^{-1}, and *i* 307 cm^{-1}. After etching, only RBMs lower than 200 cm^{-1} (peaks *a*, *b*, and *c*) are still abundant. The peak at 300 cm^{-1} is substrate related. This sample was so completely etched that it is difficult to assess the selectivity from the RBM spectra. Here, the small-diameter semiconductors have been etched away along with the metallic nanotubes. Semiconducting nanotubes are still present, but they are at the same time large-diameter nanotubes.

The G band area in Figure 3(b) reveals more information. Initially, relatively distinct G− peaks can be identified at 1504, 1523, and 1540 cm^{-1}. The 1540 and 1523 cm^{-1}

peaks are probably semiconducting, while the 1504 cm^{-1} peak is probably metallic (see SI for details). More G− peaks are present but cannot be directly identified due to overlap. Below ~1500 cm^{-1}, however, this overlapping signal is due almost entirely to m-CNTs.[71] After etching, the three distinct peaks also entirely disappear, while a possible doublet peak composed of 1562 and 1570 cm^{-1} is revealed. These two peaks are very likely semiconducting and were obscured, presumably by large-diameter metallic G− peaks that have been etched away. They probably correspond respectively to the same species producing the RBM *c* and *b* peaks (see SI for more information). The loss in the overall Breit−Wigner−Fano (BWF) line shape, an asymmetric line shape thought to be characteristic of metallic nanotubes, is apparent. Here again the G− band evolution provides an independent line of evidence for metal-specific etching. The G+ peak also narrows from 3.2 meV to 1.8 meV (*i.e.*, full width at half-maximum), probably representing the narrowing distribution of nanotubes.

The D band intensity falls dramatically, with the D/G ratio falling from $I_D/I_G = 0.26$ to $I_D/I_G = 0.01$. This drop likely corresponds to the well-established and expected oxidation of defective and/or amorphous carbon and resulting improvement to CNT sample crystallinity.[25,33,61] The D band line shape before, during, and after etching is compared in the SI. Again, we observe no clear change in D band structure.

Exposing the samples to ambient air during the etching process is expected to p-dope the CNTs, so it is also important to distinguish which Raman spectral changes are due to doping and which are due to material loss *via* etching. In particular, oxygen gas and water vapor are known to affect the electrical characteristics of CNT devices, and the presence of oxygen gas has been used to tune the band gap of s-CNTs.[75] Additionally, if substantial doping does occur, we expect the Kohn anomaly resulting from electron−phonon coupling in m-CNTs to be affected.[76,77] Due to this effect, different levels of doping have been shown to change the G− width of m-CNTs, so it would be useful to distinguish whether the change in G− shape we observe is primarily due to this effect or preferential metallic destruction.

To determine the amount of doping occurring during exposure to air in our samples, we compare our spectra to the work of Kavan *et al.*, which shows how the typical electrochemical doping of both metallic and semiconducting CNTs causes the Raman intensities of RBMs and the G band to fall in intensity and shift.[78] Depending on the applied voltage, doping was found to either fill or deplete the peaks in the density of electronic states of s-CNTs and m-CNTs. Some irreversible oxidation was found to occur at large positive potential (>1.2 V), with the largest losses in G+ intensity accompanied by upshifts of up to ~20 cm^{-1} and RBM upshifts of up to ~5 cm^{-1}.[78]

In the present work, throughout all our etching temperatures, no substantial shifts to G+ frequency are shown to accompany G band intensity loss, such as in Figure 2(b). Likewise, no shifts to RBM frequencies were observed to occur simultaneously with falling RBM intensities. It therefore seems likely that the majority of the observed Raman intensity loss is due to nanotube destruction instead of doping effects, especially for small-diameter RBMs.

It is also notable that, at low etching temperatures ($T < 400$ °C), the intensity drop can occur over a period of several hours. Unless there is a high barrier for the doping, which would not be the case if it requires only physisorption, for example, one might expect the time scale of doping to be much faster. We do observe a very small, 1−2 cm^{-1} downshift of some RBMs immediately after exposure to air, and this could be doping related; but this change occurs during the first seconds of a run and is unrelated to the large drops in Raman intensity during etching. Additionally, given the unambiguous loss in BWF character after etching, accompanying loss in G+ intensity and the fact that we start with a significant amount of s-CNTs prior to etching, it seems unlikely that line width changes can be explained by doping.

We attempted to explore type and chiral selectivity using *ex situ* multiwavelength Raman at 514, 633, and 785 nm for the 400 °C etched sample, before and after etching. The data are not obtained *in situ* and come from different areas of the same sample. We only have a snapshot at some location after a fixed amount of etching. Definitive (*n*,*m*) assignment of the RBMs remains difficult, although a larger population of CNTs resonant at different wavelengths is examined. Effects beyond diameter, presumably related to chiral angle, are blatant, with several examples of close neighbors in diameter etching at different rates. However semiconductor *versus* metal type selectivity proved difficult to verify, mainly because the resonant nanotubes at 633 and 785 nm turned out to be primarily semiconducting to begin with, but there are some specific examples of faster etch rates for peaks that could be tentatively assigned to metallic peaks. A detailed discussion is included in the SI. Here we provide a brief summary with respect to type selectivity.

The results at 514 nm were for the most part similar to 532 nm. At 514 nm (see SI), RBM *g* is probably semiconducting, and peaks *h* to *k* are probably metallic. Since it is a larger diameter, the relative robustness of peak *g* might be consistent with semiconductors resisting etching more than metallic. The G− line shape loses its metallic BWF line shape and appears more semiconducting. Finally the 2D band, which is initially split into two peaks, retains only the large-frequency peak. This could have various causes, but speculatively might be because a metallic 2D peak is lost or due to the loss of certain CNT diameters.

Interestingly, RBM *i* resists etching, yet our most likely assignment for it is metallic. A possible assignment for this peak is to the (8,8) species, despite armchair nanotubes being expected to etch rapidly.[45]

At 633 nm (see SI) RBM *e* is more resistant to etching than RBMs *c* and *d*, despite being a smaller diameter nanotube. This might be because *e* is semiconducting, and a reasonable assignment is that *c* and *d* are metallic. Chiral angle dependent rates are clear because *g*, *h*, and *i* are very close in diameter (and Raman shift), yet *h* etches slowly, while *g* and *i* etch quickly. Changes to the semiconducting/metal character of the G− are not clearly visible here at 633 nm.

At 785 nm (see SI), RBM *d* is a semiconducting nanotube and is quite resistant to etching. Some RBM peaks appear to etch faster and can be assigned to metallic tubes, but there are also possible semiconductor assignments as well. After etching, the G− band is characteristic mainly of large-diameter semiconductors and arguably may have lost some metallic character, but this change, if real, is subtle at best. We conclude that the *ex situ* measurements do not disagree with the *in situ* data, but nor do they demonstrate clear type selectivity.

The *in situ* data also allow us to explore the dynamics of etching, and this was also characterized by extracting the integrated intensities of *in situ* Raman bands as a function of time for various temperatures. A challenge for such measurements is background subtraction, which can be a large source of error in the evolution curves. For background subtraction, we employed a simple trapezoidal background correction algorithm, described in previous work[65] and illustrated in the SI. As described above the integrated intensities were further normalized against the first-order Si band to compensate for any drift in illumination intensity or collection efficiency. This is a good approach as long as the film is very transparent. In Figure 4, the G (consisting of both G+ and G−) and D band evolution is presented with the integrated intensity normalized so that its initial intensity is unity. The change in resonance window for 300 °C is small ($k_BT \approx 0.03$ eV) and comparable to a 6 nm decrease in incident wavelength.

We also analyzed RBMs in this way, and the results are broadly consistent with the preferential etching of metallic nanotubes, but the background subtraction for RBMs is much less robust than for G and D bands because of the uneven background in the RBM spectral range (see SI). This means that the quantitative evolution of the extracted intensities faithfully represents the G and D bands, but is less certain for the RBM bands. The trends in the evolution curves with temperature are smoothly varying. We note that one curve does not fit perfectly in Figure 4, namely, the sample etched at 500 °C (open squares). This is because this sample was grown in a different batch of samples with

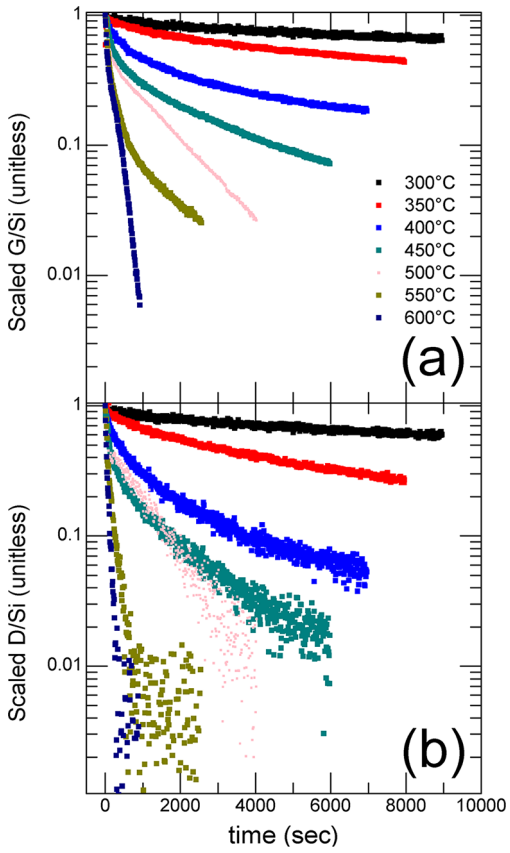

Figure 4. Time evolution plots of the integrated Raman intensities for the (a) G band and (b) D band at different etching temperatures. The samples are etched at 50 °C increments from 300 °C (top) to 600 °C (bottom). The 500 °C sample had a lower pre-etch I_D/I_G ratio. Spectra have been scaled with respect to the first-order Si intensity of the substrate in order to reduce the effect of mechanical drift on the Raman signal and normalized to 1 at $t = 0$.

a somewhat lower starting D/G ratio and different starting RBM intensities than the other samples, which affected the evolution at late times. Despite this different initial state, it does fit the general trend very well at early times.

Across all temperatures, D band etching occurred more rapidly than G band etching, and as expected, all etching rates increase with temperature.

None of the G band and D band evolution curves could be fit with a single-exponential decay function. There are at least two etching phases in each curve. Therefore, as shown in Figure 5(a) for the $T = 450$ °C etch, biexponential decay (light gray) does fit reasonably well. One fast (wine) and one slow (violet) exponential function are fit, such that the scaled intensity $I(t)$ is $I(t) = I_{fast} + I_{slow} = A_{fast}\exp(-t/\tau_{fast}) + A_{slow}\exp(-t/\tau_{slow})$, where A_{fast} and A_{slow} are proportionality constants, τ_{fast} and τ_{slow} are time constants, and t is the time elapsed from when air input begins. For the $T = 300$ to 600 °C samples, τ_{slow} varied from 16 900 s to 250 s and τ_{fast} varied from 1200 s to 35 s for the G bands. For some etching temperatures, the fast etching phase may actually contain more than one exponential, so the biexponential fit is only an

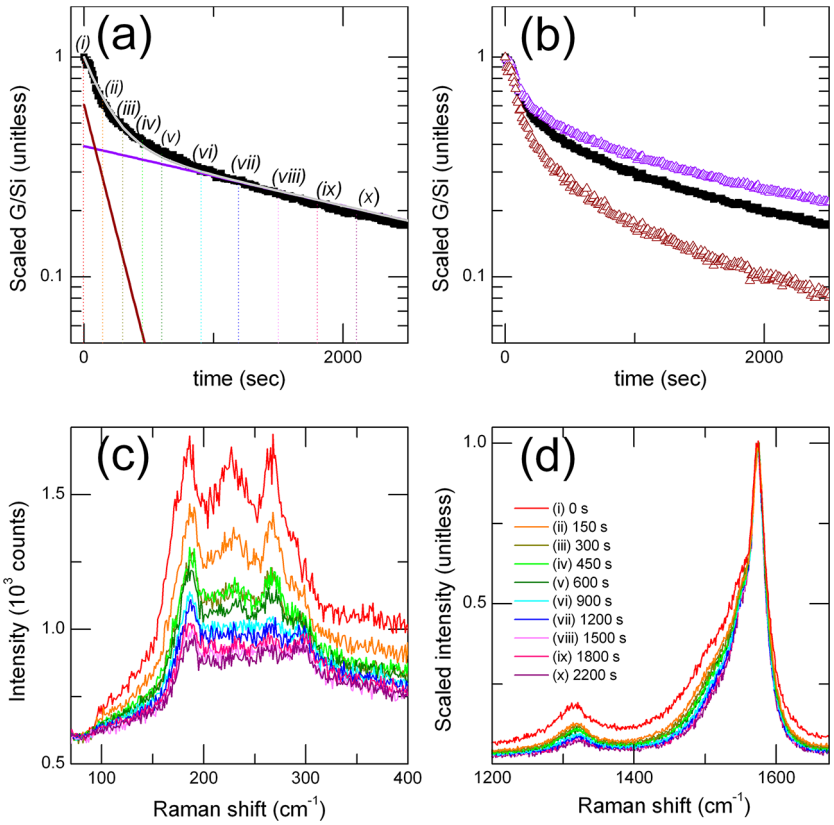

Figure 5. (a) Typical biexponential fit (light gray) of the G band signal (black, normalized to the Si intensity) for the 450 °C etched sample. Slow (violet) and fast (wine) decay components are indicated. The respective time scales for the slow and fast components are $\tau = 3203 \pm 25$ s and $\tau = 188 \pm 3$ s. (b) Comparison of G band decay: Total G band signal (black) *versus* metallic G− signal (wine, from 1456 to 1476 cm^{-1}) and G+ signal (violet, from 1565 to 1585 cm^{-1}) for the 450 °C etched sample. Corresponding (c) RBM and (d) D and G spectra for each of the 10 etching times shown in (a).

approximation, although for other temperatures the fit was excellent. Also, for comparison with total G band evolution, Figure 5(b) shows the evolution of the low-frequency, metallic G− peaks from 1456 to 1476 cm^{-1} (wine triangles) and that of the G+ peak from 1565 to 1585 cm^{-1} (violet triangles). As expected, the metallic peaks decay more rapidly.

There is some evidence that the fast and slow components represent different nanotube populations. Spectrally, as seen in Figure 5(b) and (c), by the time when I_{fast} drops close to 0 (*i.e.*, at point (vi)), in all samples, RBM *c* is the dominant peak and, assuming that G band contribution from non-CNT sources at this stage of the etch is low, I_{slow} at least roughly tracks the decay of RBM *c*. After I_{fast} drops close to 0, the G line shape appears much more stable, indicating that the majority of metal etching has already occurred during this first etching stage. It follows that the amount of metal/semiconductor etching can be optimized by stopping air input at different times. Roughly speaking, one can conclude that the fast component corresponds to the phase when the G band narrows most, and many species are selectively lost in the RBM region, while the slow component corresponds to the phase when the remaining G band and RBM band intensities simply decrease uniformly.

Our samples are highly bundled, so we should consider what effect bundling has on the kinetic Raman spectra and the observed fast and slow components. While the fraying of bundles observed in SEM may indicate that air is still efficiently getting to the core of the bundles, it is still possible that outer CNTs will etch before the inner CNTs and protect them to a degree. In CVD growth, the *a priori* expectation is that chirality, diameter, and metallicity of individual CNTs are randomly distributed within the bundle, with bundle formation occurring well after CNT nucleation. It is therefore unlikely that distinct inner and outer CNT groups within a bundle are directly responsible for the fast and slow components. This random CNT distribution within the sample should actually decrease the amount of etching selectivity, since some portion of the protected inner CNTs would consist of otherwise etch-susceptible species. More generally, CNT bundles and surface CNTs are not well organized on the substrate. So, the chirality and type dependence of etching should be enhanced for debundled and individualized nanotubes.

Debundling caused by etching may directly impact the resonance windows of different CNTs. Additionally, bundle thickness is expected to affect overall G bandwidth.[79] However, at all etching temperatures,

we do not see any significant shift in the RBM, G−, or G+ frequencies, which would indicate that a significant change to strain induced by debundling has occurred.[80] If anything, based on the aforementioned SEM images in Figure 1 and lack of D band shift, there appears to be minimal debundling, and few individual CNTs are visible once the fast component has fallen to zero and selective etching has already occurred.

One complication in trying to understand the time evolution is that at high temperatures the etch rate becomes so fast that it is no longer possible to ignore the time it takes to change over the gas composition from reducing to oxidizing. The chamber has an internal volume of ~29 cm^3, and the supply lines have a volume of ~4 cm^3. The air is introduced at a flow rate of 16 sccm, meaning it should take a time scale on the order of 90 s to turn over the gas composition. Such effects do not explain the biexponential, however, as they should be negligible at low temperatures because of the slow etch rate. Furthermore, one would expect the presence of the purge gas transient to decrease the etching rate, instead of increasing it, as observed here. However, for the fastest etching rates, it is clear that one has to view the gas concentration as ramping up during the etch. For the highest temperatures, it is not a good approximation to view the gas concentrations as static.

Since the $1/\tau$ values are simply rates, the temperature dependence of these etch rates can be plotted in an activation plot as shown in Figure 6. The slow (black squares) and fast (red squares) G band etch rates are activated with energies 0.67 ± 0.05 and 0.50 ± 0.12 eV, respectively. That is, given the large uncertainty they are barely distinguishable, if at all, in activation energy. The slow (blue triangles) and fast (green triangles) D band etch rates are activated with energies of 0.79 ± 0.13 and 0.58 ± 0.13 eV, respectively. Given the large uncertainty, these too cannot be meaningfully distinguished. These energies are of the same order of magnitude for activation energies obtained in studies involving the etching of graphitic carbon.[8,29] If the fast and slow modes correspond to different populations, the difference in etching activation energy for these populations was too small to measure in our experiment.

As described in the SI, as an alternative to fitting biexponentials for the entire duration of the G and D band evolutions, one exponential could be fit at early times and one exponential could be fit at late times. Using this method, activation plots for the fast and slow phases for the G and D bands were also obtained. These energies are similar to the results obtained from the biexponential fits, indicating that the biexponential function reasonably approximates G and D evolution.

It is possible to extract and analyze certain RBM evolution curves and extract different activation energies, similar to what was accomplished for the G and D bands in Figures 5 and 6. Depending on RBM peak

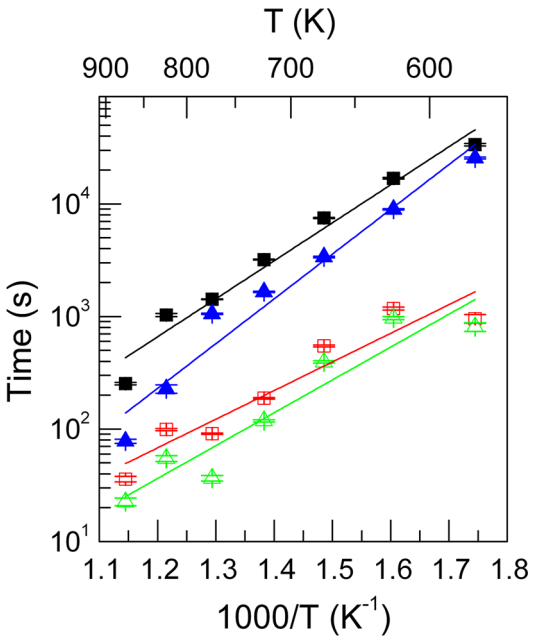

Figure 6. Activation plots for the G band slow (black square) and fast (red square) τ values and for the D band slow (blue triangle) and fast (green triangle) τ values. Activation energies are taken from the slopes of the four linear fits (lines) and are listed in the main text.

intensity, spectral background intensity, and etching rate, it was not possible to obtain evolution curves for all RBMs. However, curves from peaks *b*, *c*, *e*, *f*, and *g* identified in Figure 2 could be tracked over a variety of temperatures, with Figure 7(a) displaying the 350 °C etching case. Due to overlap, the intensities of peaks *e* and *f* were combined. Unlike the G and D bands, all the RBM curves can be roughly fit with a single-exponential function, with the assigned metallic *e* and *f* peaks (blue) etching rapidly and peak *c* (red) being the most resistant. Keeping in mind that the resonance window of the G band is larger than that of the RBMs, slow G band decay generally corresponds well with the decay of peak *c*, while fast G band decay may correspond with the averaged decay of the remaining RBM peak populations.

Some RBM-activated plots are shown in Figure 7(b). Note that due to the large signal-to-noise ratios of the RBMs, the energy uncertainties are larger than those of the G and D bands. The energies for peaks *b*, *c*, and *g* and the combined peaks *e* and *f* are respectively found to be 1.19 ± 0.69, 0.99 ± 0.23, 0.78 ± 0.20, and 0.72 ± 0.20 eV. Therefore, while the energies for the larger diameter peaks *b* and *c* may be larger than those of the other RBMs, the RBM energies cannot be meaningfully distinguished from each other or from the energies of the G and D bands, despite the substantially different etching rates of different RBMs.

This raises an interesting point about the mechanism of selectivity. One model is that selectivity in oxidation rates arises from different activation barriers. This may be true in some cases, and we may simply lack the energy resolution in the current experiment.

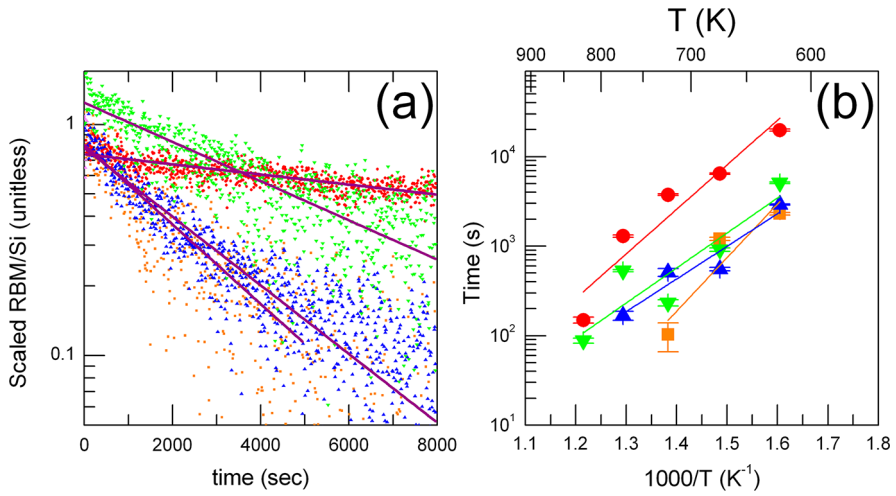

Figure 7. (a) Typical exponential fits (violet lines) of RBM band signals during etching at 350 °C. RBMs at 177 cm^{-1} ("peak *b*", orange), 192 cm^{-1} ("peak *c*", red), and 273 cm^{-1} ("peak *g*", green) are shown. The intensities of the RBM signals at 230 and 236 cm^{-1} ("peaks *e* and *f*", blue) have been combined. All signals are scaled to the Si intensity and normalized to 1 at $t = 0$. (b) Activation plots for the four RBM groups identified in part (a). Activation energies are listed in the main text.

However, this does not explain peak *c* in Figure 7, which etches much more slowly despite having a similar activation energy to the others. So at least in this case, this is evidence that selectivity is determined by the prefactor in the Arrhenius equation and not the activation energy factor.

One interpretation may be that fast etching nanotubes, which we suppose are metallic here, effectively have a higher molecular collision rate. Speculatively, this might be explained by the relative delocalization of metallic electrons on m-CNTs[81] or possibly by the higher polarizability of m-CNTs, which increases the magnitude of van der Waals interactions,[82] resulting in a larger effective cross-section. Another possibility is that metallic species are more sensitive to defects formed during growth, resulting in greater reactivity.[83,84]

Mechanisms of selectivity related to the electronic density of states near the Fermi level for m-CNTs are also often used to explain enhanced metallic etch rate.[22,38,85] For example, An *et al*. have attributed the selective reactivity of diazonium reagents with m-CNTs to the stabilization of a charge-transfer complex formed at the metallic density of states.[82,83] Likewise, the preferential etching of m-CNTs with methanol has been linked to the lower ionization potential of m-CNTs.[86] Independent density functional theory calculations have shown that semiconducting single-walled nanotubes have a lower heat of formation,[53] while unique impurity states near the Fermi level of m-CNTs act as a strong scattering center,[87] both of which result in m-CNTs being more reactive than s-CNTs.[37] Additionally, it is known that the atmospheric oxygen and water can cause charge transfer and trapping, which can affect the behavior of s-CNT and m-CNT devices differently.[75]

It is important to note that our samples have cobalt catalyst present. Cobalt oxides might also play a similar role to the nickel oxides in the carbothermic reaction very recently reported by Li *et al*., and the mechanism of selectivity may be similar in that case.[26] Catalyst particle shape[88] and catalyst reduction potential[26,27,89] may be important factors.

Recently there has been discussion that growth rates might be proportional to chiral angle.[60,90] If that were true, one might imagine that etch rates could also be proportional to chiral angle, and there is evidence for such scaling in air etching studies.[1,50] Note that this is a different argument than the local curvature radius limiting etch rates, which implies a specific, but different chiral angle dependence. The argument for growth rates proportional to chiral angle hinges on the graphene edge step density scaling with chiral angle. In etching this would be relevant if it took place from the end only. Very recent observations of oxidation in aberration-corrected environmental transmission electron microscopy show, however, that etching proceeds by attacking sidewalls more commonly.[66] Although oxidation is in some ways the opposite of growth, it would appear that the time reverse of the growth model does not match the oxidation dynamics, at least in our case.

The local curvature radius model might explain some of the data. Here, there are a large range of chiral angles visible in the RBM and/or G− spectra. However, we do not generally observe large variations in etch rate due to chiral angles when we make a tentative assignment. For example, large and small chiral angles are present in RBMs *g* to *i*, but we do not observe any large difference in etching behavior within this group (see SI). Bundling, too, may be a factor here, since the inner nanotubes are protected from gas exposure to at least some extent, which would weaken any specific chirality dependence. If that is the case, one should expect better selectivity from more debundled samples.

In general, assigning chiralities to large-diameter nanotubes *via* Raman spectroscopy is prone to error. It is possible that the etch-resistant RBM *c* corresponds to the semiconducting zigzag (16,0) species. This assignment would be compatible with a chiral angle determining the etch rate. However, there are many equally plausible assignments for that peak. Moreover, other near-zigzag peaks at small diameter can be assigned, and they do not show significantly slower etch rates. Therefore, we could not find clear evidence of the simple chiral angle rate dependence suggested by the local curvature model. If there is a simple chiral angle dependency, it is perhaps masked by semiconductor/metal type dependences and by bundling. Certainly, however, the trend of small-diameter nanotubes being etched first is clear.

CONCLUSIONS

To summarize, our *in situ* Raman spectroscopy generally supports the idea that etch rates are faster for small-diameter nanotubes. However this is only the beginning of the story. Subsets of the population persist longer than other species. Chiral angle effects are clearly present, but there is also evidence for type dependence. In particular, the *in situ* data are consistent with m-CNTs etching more rapidly than s-CNTs, and this is manifested in a biexponential of G band intensity. Extracted activation energies appear largely independent of tube chirality, leading to the conclusion that differences in etch rates are predominantly determined by other factors such as cross-section.

This selective etching approach, while suffering from the drawback of destroying a lot of material, is very simple and scalable and would be particularly interesting to integrate with gas-phase synthesis. With further study, it could have the potential to be used as a tool to produce semiconductor-enriched samples, while improving crystallinity. *In situ* tools such as *in situ* Raman can help test the mechanism of selectivity and help to optimize selectivity.

METHODS

Etching was tracked by *in situ* Raman spectroscopy as follows: samples, consisting of chemical vapor deposition produced nanotubes grown from cobalt thin film catalyst on thermally oxidized silicon wafers, were cleaved into 3 mm × 3 mm square pieces and loaded into a miniature hot-walled chemical reactor (Linkam CCR1000). A custom-built Raman spectroscopy system was used to monitor the sample *in situ* as described in previous work.[65,91] The reactor was purged in 2% H_2/Ar at 16 sccm and heated to a fixed temperature between 300 and 600 °C. Etching was initiated by pumping ambient room air with a diaphragm pump into the reactor at a flow rate of 16 sccm, and air flow was maintained for a matter of minutes or hours, depending on the etch rate. After etching, the reactor was again purged with H_2/Ar at 16 sccm and cooled to room temperature.

Raman spectroscopy was performed on all samples before, during, and after etching, always using the 532 nm laser line. Focusing conditions are important. To avoid laser heating the beam was defocused to a narrow elliptical spot roughly ∼50 μm long and ∼5 μm wide, with incident power ∼1 mW using a 50× long working distance objective. A spatially extended spot provides a stronger Raman signal than would be obtained from a point, while minimizing local heating. Given the lack of a noticeable frequency shift of the Raman first-order Si band and the carbon-related bands, local sample heating due to the laser is estimated to be less than ∼25 °C. Second, small spatial drifts in the *z* (focusing) direction can cause large drifts in the collection efficiency, and so cause artifacts in the evolution profile. To compensate, we used a separate imaging arm[63,65] built into our Raman system. This arm was used to continually refocus the laser spot between acquisitions of spectra to compensate for any drift. Furthermore, the nanotube layer was thin enough to be transparent, and we normalize the nanotube-related bands to the substrate silicon first-order band to cancel out small drifts. The result was that very smooth and reproducible evolution curves could be extracted.

Conflict of Interest: The authors declare no competing financial interest.

Supporting Information Available: Diameter and chirality assignment for radial breathing mode and G− peaks. Raman spectra of sample etched at T = 600 °C. Radial breathing mode time evolution plots. D/G ratio time evolution plots. Alternative G and D band activation plots. TEM images at low and high resolution of pre-etch material. Multiwavelength Raman spectra of sample etched at T = 400 °C. Background correction illustration. Comparison of D band line shape for sample etched at T = 550 °C. XPS spectra of pre-etch material. This material is available free of charge *via* the Internet at http://pubs.acs.org.

Acknowledgment. This work was supported by a Discovery Grant (P.F., A.L.) from the Natural Sciences and Engineering Research Council of Canada (NSERC) and a grant (A.L.) from Le Fonds de Recherche du Québec—Nature et Technologies (FRQNT). We are grateful for the assistance of Paul Marshall, Phillip Vinten, Hue Tran, Chris Kingston, and Xiaohua Wu for TEM data, Martin Couillard for HRTEM data, and Oltion Kodra for XPS data.

REFERENCES AND NOTES

1. Miyata, Y.; Kawai, T.; Miyamoto, Y.; Yanagi, K.; Maniwa, Y.; Kataura, H. Chirality-Dependent Combustion of Single-Walled Carbon Nanotubes. *J. Phys. Chem. C* **2007**, *111*, 9671–9677.
2. Hodge, S. A.; Bayazit, M. K.; Coleman, K. S.; Shaffer, M. S. P. Unweaving the Rainbow: A Review of the Relationship between Single-Walled Carbon Nanotube Molecular Structures and their Chemical Reactivity. *Chem. Soc. Rev.* **2012**, *41*, 4409–4429.
3. Borowiak-Palen, E.; Pichler, T.; Liu, X.; Knupfer, M.; Graff, A.; Jost, O.; Pompe, W.; Kalenczuk, R. J.; Fink, J. Reduced Diameter Distribution of Single-Wall Carbon Nanotubes by Selective Oxidation. *Chem. Phys. Lett.* **2002**, *363*, 567–572.
4. Chiang, I. W.; Brinson, B. E.; Huang, A. Y.; Willis, P. A.; Bronikowski, M. J.; Margrave, J. L.; Smalley, R. E.; Hauge, R. H. Purification and Characterization of Single-Wall Carbon Nanotubes (SWNTs) Obtained from the Gas-Phase Decomposition of CO (HiPco Process). *J. Phys. Chem. B* **2001**, *105*, 8297–8301.
5. Nagasawa, S.; Yudasaka, M.; Hirahara, K.; Ichihashi, T.; Iijima, S. Effect of Oxidation on Single-Wall Carbon Nanotubes. *Chem. Phys. Lett.* **2000**, *328*, 374–380.
6. Wiltshire, J. G.; Khlobystov, A. N.; Li, L. J.; Lyapin, S. G.; Briggs, G. A. D.; Nicholas, R. J. Comparative Studies on Acid and Thermal Based Selective Purification of HiPCO Produced Single-Walled Carbon Nanotubes. *Chem. Phys. Lett.* **2004**, *386*, 239–243.

7. Balasubramanian, K.; Burghard, M. Chemically Functionalized Carbon Nanotubes. *Small* **2005**, *1*, 180–192.
8. Brukh, R.; Mitra, S. Kinetics of Carbon Nanotube Oxidation. *J. Mater. Chem.* **2007**, *17*, 619–623.
9. Bom, D.; Andrews, R.; Jacques, D.; Anthony, J.; Chen, B.; Meier, M. S.; Selegue, J. P. Thermogravimetric Analysis of the Oxidation of Multiwalled Carbon Nanotubes: Evidence for the Role of Defect Sites in Carbon Nanotube Chemistry. *Nano Lett.* **2002**, *2*, 615–619.
10. Dillon, A. C.; Gennett, T.; Jones, K. M.; Alleman, J. L.; Parilla, P. A.; Heben, M. J. A Simple and Complete Purification of Single-Walled Carbon Nanotube Materials. *Adv. Mater.* **1999**, *11*, 1354–1358.
11. Yang, S.; Rafael Castilleja, J.; Barrera, E. V.; Lozano, K. Thermal Analysis of an Acrylonitrile-Butadiene-Styrene/SWNT Composite. *Polym. Degrad. Stab.* **2004**, *83*, 383–388.
12. Arepalli, S.; Nikolaev, P.; Gorelik, O.; Hadjiev, V. G.; Holmes, W.; Files, B.; Yowell, L. Protocol for the Characterization of Single-Wall Carbon Nanotube Material Quality. *Carbon* **2004**, *42*, 1783–1791.
13. Futaba, D. N.; Hata, K.; Yamada, T.; Mizuno, K.; Yumura, M.; Iijima, S. Kinetics of Water-Assisted Single-Walled Carbon Nanotube Synthesis Revealed by a Time-Evolution Analysis. *Phys. Rev. Lett.* **2005**, *95*, 056104.
14. Magrez, A.; Seo, J. W.; Kuznetsov, V. L.; Forro, L. Evidence of an Equimolar C_2H_2-CO_2 Reaction in the Synthesis of Carbon Nanotubes. *Angew. Chem.* **2007**, *119*, 445–448.
15. Zhang, G.; Mann, D.; Zhang, L.; Javey, A.; Li, Y.; Yenilmez, E.; Wang, Q.; McVittie, J. P.; Nishi, Y.; Gibbons, J.; *et al*. Ultra-High-Yield Growth of Vertical Single-Walled Carbon Nanotubes: Hidden Roles of Hydrogen and Oxygen. *Proc. Natl. Acad. Sci. U.S.A.* **2005**, *102*, 16141–16145.
16. Xu, Y.; Peng, H.; Hauge, R. H.; Smalley, R. E. Controlled Multistep Purification of Single-Walled Carbon Nanotubes. *Nano Lett.* **2005**, *5*, 163–168.
17. Nikolaev, P.; Bronikowski, M. J.; Bradley, R. K.; Rohmund, F.; Colbert, D. T.; Smith, K. A.; Smalley, R. E. Gas-Phase Catalytic Growth of Single-Walled Carbon Nanotubes from Carbon Monoxide. *Chem. Phys. Lett.* **1999**, *313*, 91–97.
18. Nasibulin, A. G.; Brown, D. P.; Queipo, P.; Gonzalez, D.; Jiang, H.; Kauppinen, E. I. An Essential Role of CO_2 and H_2O during Single-Walled CNT Synthesis from Carbon Monoxide. *Chem. Phys. Lett.* **2006**, *417*, 179–184.
19. Huang, J.; Zhang, Q.; Zhao, M.; Wei, F. The Release of Free Standing Vertically-Aligned Carbon Nanotube Arrays from a Substrate Using CO_2 Oxidation. *Carbon* **2010**, *48*, 1441–1450.
20. Corthals, S.; Van Noyen, J.; Geboers, J.; Vosch, T.; Liang, D.; Ke, X.; Hofkens, J.; Van Tendeloo, G.; Jacobs, P.; Sels, B. The Beneficial Effect of CO_2 in the Low Temperature Synthesis of High Quality Carbon Nanofibers and Thin Multiwalled Carbon Nanotubes from CH_4 Over Ni Catalysts. *Carbon* **2012**, *50*, 372–384.
21. Chen, Z.; Ziegler, K. J.; Shaver, J.; Hauge, R. H.; Smalley, R. E. Cutting of Single-Walled Carbon Nanotubes by Ozonolysis. *J. Phys. Chem. B* **2006**, *110*, 11624–11627.
22. Yu, B.; Liu, C.; Hou, P.; Tian, Y.; Li, S.; Liu, B.; Li, F.; Kauppinen, E. I.; Cheng, H. Bulk Synthesis of Large Diameter Semiconducting Single-Walled Carbon Nanotubes by Oxygen-Assisted Floating Catalyst Chemical Vapor Deposition. *J. Am. Chem. Soc.* **2011**, *133*, 5232–5235.
23. Yu, B.; Hou, P.; Li, F.; Liu, B.; Liu, C.; Cheng, H. Selective Removal of Metallic Single-Walled Carbon Nanotubes by Combined *in Situ* and Post-Synthesis Oxidation. *Carbon* **2010**, *48*, 2941–2947.
24. Hersam, M. C. Progress Towards Monodisperse Single-Walled Carbon Nanotubes. *Nat. Nanotechnol.* **2008**, *3*, 387–394.
25. Lukaszczuk, P.; Mijowska, E.; Kalenczuk, R. Selective Oxidation of Metallic Single-Walled Carbon Nanotubes. *Chem. Pap.* **2013**, *10*), 1–5.
26. Li, S.; Liu, C.; Hou, P.; Sun, D.; Cheng, H. Enrichment of Semiconducting Single-Walled Carbon Nanotubes by Carbothermic Reaction for Use in All-Nanotube Field Effect Transistors. *ACS Nano* **2012**, *6*, 9657–9661.
27. Zhou, W.; Zhan, S.; Ding, L.; Liu, J. General Rules for Selective Growth of Enriched Semiconducting Single Walled Carbon Nanotubes with Water Vapor as *in Situ* Etchant. *J. Am. Chem. Soc.* **2012**, *134*, 14019–14026.
28. Valuev, I.; Norman, G.; Shub, B. Mechanisms of the Oxidation of Defect-Free Surfaces of Carbon Nanostructures: The Influence of Surface Curvature. *Russ. J. Phys. Chem. B* **2011**, *5*, 156–162.
29. Hahn, J. R. Kinetic Study of Graphite Oxidation along Two Lattice Directions. *Carbon* **2005**, *43*, 1506–1511.
30. Jhi, S.; Louie, S. G.; Cohen, M. L. Electronic Properties of Oxidized Carbon Nanotubes. *Phys. Rev. Lett.* **2000**, *85*, 1710–1713.
31. Lee, S. M.; Lee, Y. H.; Hwang, Y. G.; Hahn, J. R.; Kang, H. Defect-Induced Oxidation of Graphite. *Phys. Rev. Lett.* **1999**, *82*, 217–220.
32. Sorescu, D. C.; Jordan, K. D.; Avouris, P. Theoretical Study of Oxygen Adsorption on Graphite and the (8,0) Single-Walled Carbon Nanotube. *J. Phys. Chem. B* **2001**, *105*, 11227–11232.
33. Osswald, S.; Flahaut, E.; Gogotsi, Y. *In Situ* Raman Spectroscopy Study of Oxidation of Double- and Single-Wall Carbon Nanotubes. *Chem. Mater.* **2006**, *18*, 1525–1533.
34. Collins, P. G.; Arnold, M. S.; Avouris, P. Engineering Carbon Nanotubes and Nanotube Circuits using Electrical Breakdown. *Science* **2001**, *292*, 706–709.
35. Zhang, H.; Liu, Y.; Cao, L.; Wei, D.; Wang, Y.; Kajiura, H.; Li, Y.; Noda, K.; Luo, G.; Wang, L.; *et al*. A Facile, Low-Cost, and Scalable Method of Selective Etching of Semiconducting Single-Walled Carbon Nanotubes by a Gas Reaction. *Adv. Mater.* **2009**, *21*, 813–816.
36. Hassanien, A.; Tokumoto, M.; Umek, P.; Vrbanic, D.; Mozetic, M.; Mihailovic, D.; Venturini, P.; Pejovnik, S. Selective Etching of Metallic Single-Wall Carbon Nanotubes with Hydrogen Plasma. *Nanotechnology* **2005**, *16*, 278.
37. Zhang, G.; Qi, P.; Wang, X.; Lu, Y.; Li, X.; Tu, R.; Bangsaruntip, S.; Mann, D.; Zhang, L.; Dai, H. Selective Etching of Metallic Carbon Nanotubes by Gas-Phase Reaction. *Science* **2006**, *314*, 974–977.
38. Yang, C.; An, K. H.; Park, J. S.; Park, K. A.; Lim, S. C.; Cho, S.; Lee, Y. S.; Park, W.; Park, C. Y.; Lee, Y. H. Preferential Etching of Metallic Single-Walled Carbon Nanotubes with Small Diameter by Fluorine Gas. *Phys. Rev. B* **2006**, *73*, 075419.
39. Zhou, W.; Ooi, Y. H.; Russo, R.; Papanek, P.; Luzzi, D. E.; Fischer, J. E.; Bronikowski, M. J.; Willis, P. A.; Smalley, R. E. Structural Characterization and Diameter-Dependent Oxidative Stability of Single Wall Carbon Nanotubes Synthesized by the Catalytic Decomposition of CO. *Chem. Phys. Lett.* **2001**, *350*, 6–14.
40. Menna, E.; Della Negra, F.; Dalla Fontana, M.; Meneghetti, M. Selectivity of Chemical Oxidation Attack of Single-Wall Carbon Nanotubes in Solution. *Phys. Rev. B* **2003**, *68*, 193412.
41. Moon, C.; Kim, Y.; Lee, E.; Jin, Y.; Chang, K. J. Mechanism for Oxidative Etching in Carbon Nanotubes. *Phys. Rev. B* **2002**, *65*, 155401.
42. An, K. H.; Park, J. S.; Yang, C.; Jeong, S. Y.; Lim, S. C.; Kang, C.; Son, J.; Jeong, M. S.; Lee, Y. H. A Diameter-Selective Attack of Metallic Carbon Nanotubes by Nitronium Ions. *J. Am. Chem. Soc.* **2005**, *127*, 5196–5203.
43. Ye, J. T.; Tang, Z. K. Raman Spectra and Thermal Stability Analysis of 0.4nm Freestanding Single-Walled Carbon Nanotubes. *Phys. Rev. B* **2005**, *72*, 045414.
44. Kawai, T.; Miyamoto, Y. Chirality-Dependent C-C Bond Breaking of Carbon Nanotubes by Cyclo-Addition of Oxygen Molecule. *Chem. Phys. Lett.* **2008**, *453*, 256–261.
45. Miyata, Y.; Kawai, T.; Miyamoto, Y.; Yanagi, K.; Maniwa, Y.; Kataura, H. Bond-Curvature Effect on Burning of Single-Wall Carbon Nanotubes. *Phys. Status Solidi B* **2007**, *244*, 4035–4039.
46. Miyata, Y.; Maniwa, Y.; Kataura, H. Selective Oxidation of Semiconducting Single-Wall Carbon Nanotubes by Hydrogen Peroxide. *J. Phys. Chem. B* **2006**, *110*, 25–29.
47. Kroes, J. M. H.; Pietrucci, F.; Curioni, A.; Jaafar, R.; Gröning, O.; Andreoni, W. Atomic Oxygen Chemisorption on Carbon Nanotubes Revisited with Theory and Experiment. *J. Phys. Chem. C* **2013**, *117*, 1948–1954.

48. Doyle, C. D.; Rocha, J. R.; Weisman, R. B.; Tour, J. M. Structure-Dependent Reactivity of Semiconducting Single-Walled Carbon Nanotubes with Benzenediazonium Salts. *J. Am. Chem. Soc.* **2008**, *130*, 6795–6800.
49. Song, J. W.; Seo, H. W.; Park, J. K.; Kim, J. E.; Choi, D. G.; Han, C. S. Selective Removal of Metallic SWNTs using Microwave Radiation. *Curr. Appl. Phys.* **2008**, *8*, 725–728.
50. Huang, H.; Maruyama, R.; Noda, K.; Kajiura, H.; Kadono, K. Preferential Destruction of Metallic Single-Walled Carbon Nanotubes by Laser Irradiation. *J. Phys. Chem. B* **2006**, *110*, 7316–7320.
51. Gomez, L. M.; Kumar, A.; Zhang, Y.; Ryu, K.; Badmaev, A.; Zhou, C. Scalable Light-Induced Metal to Semiconductor Conversion of Carbon Nanotubes. *Nano Lett.* **2009**, *9*, 3592–3598.
52. Hong, G.; Zhang, B.; Peng, B.; Zhang, J.; Choi, W. M.; Choi, J.; Kim, J. M.; Liu, Z. Direct Growth of Semiconducting Single-Walled Carbon Nanotube Array. *J. Am. Chem. Soc.* **2009**, *131*, 14642–14643.
53. Li, Y.; Peng, S.; Mann, D.; Cao, J.; Tu, R.; Cho, K. J.; Dai, H. On the Origin of Preferential Growth of Semiconducting Single-Walled Carbon Nanotubes. *J. Phys. Chem. B* **2005**, *109*, 6968–6971.
54. Okazaki, K.; Nakato, Y.; Murakoshi, K. Absolute Potential of the Fermi Level of Isolated Single-Walled Carbon Nanotubes. *Phys. Rev. B* **2003**, *68*, 035434.
55. Suzuki, S.; Watanabe, Y.; Homma, Y.; Fukuba, S.; Heun, S.; Locatelli, A. Work Functions of Individual Single-Walled Carbon Nanotubes. *Appl. Phys. Lett.* **2004**, *85*, 127–129.
56. Kang, S. J.; Song, Y.; Yi, Y.; Choi, W. M.; Yoon, S.; Choi, J. Work-Function Engineering of Carbon Nanotube Transparent Conductive Films. *Carbon* **2010**, *48*, 520–524.
57. Xu, S.; Yuan, G.; Li, C.; Liu, W.; Mimura, H. Modulation of the Work Function of Capped Single-Walled Carbon Nanotube by Alkali-Metal Adsorption: A Theoretical Study. *J. Phys. Chem. C* **2011**, *115*, 8928–8933.
58. Seo, K.; Kim, C.; Choi, Y. S.; Park, K. A.; Lee, Y. H.; Kim, B. Tuning Chirality of Single-Wall Carbon Nanotubes by Selective Etching with Carbon Dioxide. *J. Am. Chem. Soc.* **2003**, *125*, 13946–13947.
59. Chiashi, S.; Kohno, M.; Takata, Y.; Maruyama, S. Localized Synthesis of Single-Walled Carbon Nanotubes on Silicon Substrates by a Laser Heating Catalytic CVD. *J. Phys.: Conf. Ser.* **2007**, *59*, 155.
60. Rao, R.; Liptak, D.; Cherukuri, T.; Yakobson, B. I.; Maruyama, B. *In Situ* Evidence for Chirality-Dependent Growth Rates of Individual Carbon Nanotubes. *Nat. Mater.* **2012**, *11*, 213–216.
61. Osswald, S.; Havel, M.; Gogotsi, Y. Monitoring Oxidation of Multiwalled Carbon Nanotubes by Raman Spectroscopy. *J. Raman Spectrosc.* **2007**, *38*, 728–736.
62. Pauzauskie, P. J.; Jamshidi, A.; Zaug, J. M.; Baker, S.; Han, T. Y. -.; Satcher, J. H.; Wu, M. C. *In Situ* Raman Spectroscopy of COOH-Functionalized SWCNTs Trapped with Optoelectronic Tweezers. *Adv. OptoElectron.* **2012**, *2012*, 4.
63. Kaminska, K.; Lefebvre, J.; Austing, D. G.; Finnie, P. Real-Time *in Situ* Raman Imaging of Carbon Nanotube Growth. *Nanotechnology* **2007**, *18*, 165707.
64. Picher, M.; Anglaret, E.; Arenal, R.; Jourdain, V. Self-Deactivation of Single-Walled Carbon Nanotube Growth Studied by *in Situ* Raman Measurements. *Nano Lett.* **2009**, *9*, 542–547.
65. Li-Pook-Than, A.; Lefebvre, J.; Finnie, P. Phases of Carbon Nanotube Growth and Population Evolution from *in Situ* Raman Spectroscopy during Chemical Vapor Deposition. *J. Phys. Chem. C* **2010**, *114*, 11018–11025.
66. Koh, A. L.; Gidcumb, E.; Zhou, O.; Sinclair, R. Observations of Carbon Nanotube Oxidation in an Aberration-Corrected Environmental Transmission Electron Microscope. *ACS Nano* **2013**, *7*, 2566–2572.
67. Raravikar, N. R.; Keblinski, P.; Rao, A. M.; Dresselhaus, M. S.; Schadler, L. S.; Ajayan, P. M. Temperature Dependence of Radial Breathing Mode Raman Frequency of Single-Walled Carbon Nanotubes. *Phys. Rev. B* **2002**, *66*, 235424.
68. Araujo, P. T.; Pesce, P. B. C.; Dresselhaus, M. S.; Sato, K.; Saito, R.; Jorio, A. Resonance Raman Spectroscopy of the Radial Breathing Modes in Carbon Nanotubes. *Phys. E* **2010**, *42*, 1251–1261.
69. Qu, L.; Du, F.; Dai, L. Preferential Syntheses of Semiconducting Vertically Aligned Single-Walled Carbon Nanotubes for Direct Use in FETs. *Nano Lett.* **2008**, *8*, 2682–2687.
70. Telg, H.; Duque, J. G.; Staiger, M.; Tu, X.; Hennrich, F.; Kappes, M. M.; Zheng, M.; Maultzsch, J.; Thomsen, C.; Doorn, S. K. Chiral Index Dependence of the G+ and G− Raman Modes in Semiconducting Carbon Nanotubes. *ACS Nano* **2012**, *6*, 904–911.
71. Dresselhaus, M. S.; Dresselhaus, G.; Saito, R.; Jorio, A. Raman Spectroscopy of Carbon Nanotubes. *Phys. Rep.* **2005**, *409*, 47–99.
72. Jorio, A.; Souza Filho, A. G.; Dresselhaus, G.; Dresselhaus, M. S.; Swan, A. K.; Unlu, M. S.; Goldberg, B. B.; Pimenta, M. A.; Hafner, J. H.; Lieber, C. M.; *et al*. G-Band Resonant Raman Study of 62 Isolated Single-Wall Carbon Nanotubes. *Phys. Rev. B* **2002**, *65*, 155412.
73. Qiu, H.; Maeda, Y.; Akasaka, T. Facile and Scalable Route for Highly Efficient Enrichment of Semiconducting Single-Walled Carbon Nanotubes. *J. Am. Chem. Soc.* **2009**, *131*, 16529–16533.
74. Saito, R.; Fantini, C.; Jiang, J. In *Excitonic States and Resonance Raman Spectroscopy of Single-Wall Carbon Nanotubes*; Jorio, A., Dresselhaus, G., Dresselhaus, M. S., Eds.; *Carbon Nanotubes: Advanced Topics in the Synthesis, Structure, Properties and Applications* (Topics in Applied Physics); Springer-Verlag: Berlin, 2008; Vol. 111, p 251.
75. McClain, D.; Thomas, N.; Youkey, S.; Schaller, R.; Jiao, J.; O'Brien, K. P. Impact of Oxygen Adsorption on a Population of Mass Produced Carbon Nanotube Field Effect Transistors. *Carbon* **2009**, *47*, 1493–1500.
76. Caudal, N.; Saitta, A. M.; Lazzeri, M.; Mauri, F. Kohn Anomalies and Nonadiabaticity in Doped Carbon Nanotubes. *Phys. Rev. B* **2007**, *75*, 115423.
77. Farhat, H.; Son, H.; Samsonidze, G. G.; Reich, S.; Dresselhaus, M. S.; Kong, J. Phonon Softening in Individual Metallic Carbon Nanotubes Due to the Kohn Anomaly. *Phys. Rev. Lett.* **2007**, *99*, 145506.
78. Kavan, L.; Rapta, P.; Dunsch, L.; Bronikowski, M. J.; Willis, P.; Smalley, R. E. Electrochemical Tuning of Electronic Structure of Single-Walled Carbon Nanotubes: In-Situ Raman and Vis-NIR Study. *J. Phys. Chem. B* **2001**, *105*, 10764–10771.
79. Mews, A.; Jiang, C.; Schuessler, T.; Philipp, G.; Fan, Y.; Burghard, M. Raman Investigation of Single Oxidized Carbon Nanotubes. *Isr. J. Chem.* **2001**, *41*, 15–22.
80. Kumar, R.; Cronin, S. B. Raman Scattering of Carbon Nanotube Bundles Under Axial Strain and Strain-Induced Debundling. *Phys. Rev. B* **2007**, *75*, 155421.
81. Usrey, M. L.; Lippmann, E. S.; Strano, M. S. Evidence for a Two-Step Mechanism in Electronically Selective Single-Walled Carbon Nanotube Reactions. *J. Am. Chem. Soc.* **2005**, *127*, 16129–16135.
82. Lu, J.; Nagase, S.; Zhang, X.; Wang, D.; Ni, M.; Maeda, Y.; Wakahara, T.; Nakahodo, T.; Tsuchiya, T.; Akasaka, T.; *et al*. Selective Interaction of Large or Charge-Transfer Aromatic Molecules with Metallic Single-Wall Carbon Nanotubes: Critical Role of the Molecular Size and Orientation. *J. Am. Chem. Soc.* **2006**, *128*, 5114–5118.
83. An, L.; Fu, Q.; Lu, C.; Liu, J. A Simple Chemical Route to Selectively Eliminate Metallic Carbon Nanotubes in Nanotube Network Devices. *J. Am. Chem. Soc.* **2004**, *126*, 10520–10521.
84. Choubak, S.; Biron, M.; Levesque, P. L.; Martel, R.; Desjardins, P. No Graphene Etching in Purified Hydrogen. *J. Phys. Chem. Lett.* **2013**, *4*, 1100–1103.
85. Strano, M. S.; Dyke, C. A.; Usrey, M. L.; Barone, P. W.; Allen, M. J.; Shan, H.; Kittrell, C.; Hauge, R. H.; Tour, J. M.; Smalley, R. E. Electronic Structure Control of Single-Walled Carbon Nanotube Functionalization. *Science* **2003**, *301*, 1519–1522.
86. Ding, L.; Tselev, A.; Wang, J.; Yuan, D.; Chu, H.; McNicholas, T. P.; Li, Y.; Liu, J. Selective Growth of Well-Aligned Semiconducting Single-Walled Carbon Nanotubes. *Nano Lett.* **2009**, *9*, 800–805.
87. Park, H.; Zhao, J.; Lu, J. P. Distinct Properties of Single-Wall Carbon Nanotubes with Monovalent Sidewall Additions. *Nanotechnology* **2005**, *16*, 635–638.

88. Harutyunyan, A. R.; Chen, G.; Paronyan, T. M.; Pigos, E. M.; Kuznetsov, O. A.; Hewaparakrama, K.; Kim, S. M.; Zakharov, D.; Stach, E. A.; Sumanasekera, G. U. Preferential Growth of Single-Walled Carbon Nanotubes with Metallic Conductivity. *Science* **2009**, *326*, 116–120.
89. Lee, J. H.; Shin, J. H.; Kim, Y. H.; Park, S. M.; Alegaonkar, P. S.; Yoo, J. A New Method of Carbon-Nanotube Patterning Using Reduction Potentials. *Adv. Mater.* **2009**, *21*, 1257–1260.
90. Ding, F.; Harutyunyan, A. R.; Yakobson, B. I. Dislocation Theory of Chirality-Controlled Nanotube Growth. *Proc. Natl. Acad. Sci.* **2009**, *106*, 2506–2509.
91. Finnie, P.; Li-Pook-Than, A.; Lefebvre, J.; Austing, D. G. Optimization of Methane Cold Wall Chemical Vapor Deposition for the Production of Single Walled Carbon Nanotubes and Devices. *Carbon* **2006**, *44*, 3199–3206.